Solar-blind deep-UV band-pass filter (250 - 350 nm) consisting of a metal nano-grid fabricated by nanoimprint lithography

Wen-Di Li and Stephen Y. Chou*

NanoStructures Laboratory, Department of Electrical Engineering, Princeton University, Princeton, NJ 08544, USA
**chou@Princeton.EDU*

Abstract: We designed, fabricated and demonstrated a solar-blind deep-UV pass filter, that has a measured optical performance of a 27% transmission peak at 290 nm, a pass-band width of 100 nm (from 250 to 350 nm), and a 20dB rejection ratio between deep-UV wavelength and visible wavelength. The filter consists of an aluminum nano-grid, which was made by coating 20 nm Al on a SiO_2 square grid with 190 nm pitch, 30 nm linewidth and 250 nm depth. The performances agree with a rigorous coupled wave analysis. The wavelength for the peak transmission and the pass-bandwidth can be tuned through adjusting the metal nano-grid dimensions. The filter was fabricated by nanoimprint lithography, hence is large area and low cost. Combining with Si photodetectors, the filter offers simple yet effective and low cost solar-blind deep-UV detection at either a single device or large-area complex integrated imaging array level.

©2010 Optical Society of America

OCIS codes: (040.7190) Ultraviolet; (050.6624) Subwavelength structures; (130.7408) Wavelength filtering devices; (220.4241) Nanostructure fabrication.

References and links

1. T. Oshima, T. Okuno, N. Arai, N. Suzuki, H. Hino, and S. Fujita, "Flame Detection by a beta-Ga2O3-Based Sensor," Jpn. J. Appl. Phys. **48**(1), 011605 (2009).
2. E. V. Gorokhov, A. N. Magunov, V. S. Feshchenko, and A. A. Altukhov, "Solar-blind UV flame detector based on natural diamond," Instrum. Exp. Tech. **51**(2), 280–283 (2008).
3. A. Y. Hudeish, C. K. Tan, A. A. Aziz, and Z. Hassan, "A chemical sensor based on AlGaN," Functional Materials and Devices **517**, 33–36 (2006).
4. J. T. Clarke, W. R. Skinner, M. B. Vincent, T. Irgang, V. Suratkal, H. Grassl, and J. T. Trauger, "Laboratory studies of alkali metal filter deposition, ultraviolet transmission, and visible blocking," Appl. Opt. **38**(9), 1803–1813 (1999).
5. G. Chen, Z. Y. Xu, H. P. Ding, and B. M. Sadler, "Path loss modeling and performance trade-off study for short-range non-line-of-sight ultraviolet communications," Opt. Express **17**(5), 3929–3940 (2009).
6. Z. Y. Xu, and B. M. Sadler, "Ultraviolet communications: Potential and state-of-the-art," IEEE Commun. Mag. **46**(5), 67–73 (2008).
7. M. Razeghi, and R. McClintock, "A review of III-nitride research at the Center for Quantum Devices," J. Cryst. Growth **311**(10), 3067–3074 (2009).
8. R. McClintock, K. Mayes, A. Yasan, D. Shiell, P. Kung, and M. Razeghi, "320x256 solar-blind focal plane arrays based on $Al_xGa_{1-x}N$," Appl. Phys. Lett. **86**(1), 011117 (2005).
9. F. Moscatelli, "Silicon carbide for UV, alpha, beta and X-ray detectors: Results and perspectives," Nuclear Instruments & Methods in Physics Research Section a-Accelerators Spectrometers Detectors and Associated Equipment **583**(1), 157–161 (2007).
10. J. Xing, E. Guo, K. J. Jin, H. B. Lu, J. Wen, and G. Z. Yang, "Solar-blind deep-ultraviolet photodetectors based on an LaAlO(3) single crystal," Opt. Lett. **34**(11), 1675–1677 (2009).
11. Y. Z. Jin, J. P. Wang, B. Q. Sun, J. C. Blakesley, and N. C. Greenham, "Solution-processed ultraviolet photodetectors based on colloidal ZnO nanoparticles," Nano Lett. **8**(6), 1649–1653 (2008).
12. R. W. Wood, "Remarkable optical properties of the alkali metals," Phys. Rev. **44**(5), 353–360 (1933).
13. R. G. Safin, I. S. Gainutdinov, R. S. Sabirov, and M. K. Azamatov, "Solar-blind filter for the ultraviolet region," J. Opt. Technol. **74**(3), 208–210 (2007).
14. F. G. Haibach, A. E. Greer, M. V. Schiza, R. J. Priore, O. O. Soyemi, and M. L. Myrick, "On-line reoptimization of filter designs for multivariate optical elements," Appl. Opt. **42**(10), 1833–1838 (2003).
15. T. Tanaka, M. Akazawa, and E. Sano, "Terahertz wave filter from cascaded thin-metal-film meshes with a triangular array of hexagonal holes," Jpn. J. Appl. Phys. **43**(Part 2), L287–L289 (2004).

#120565 - $15.00 USD Received 30 Nov 2009; revised 21 Dec 2009; accepted 21 Dec 2009; published 6 Jan 2010

16. K. Jefimovs, T. Vallius, V. Kettunen, M. Kuittinen, J. Turunen, P. Vahimaa, M. Kaipiainen, and S. Nenonen, "Inductive grid filters for rejection of infrared radiation," J. Mod. Opt. **51**(11), 1651–1661 (2004).
17. H. S. Lee, Y. T. Yoon, S. S. Lee, S. H. Kim, and K. D. Lee, "Color filter based on a subwavelength patterned metal grating," Opt. Express **15**(23), 15457–15463 (2007).
18. Y. Ekinci, H. H. Solak, and C. David, "Extraordinary optical transmission in the ultraviolet region through aluminum hole arrays," Opt. Lett. **32**(2), 172–174 (2007).
19. S. Y. Chou, P. R. Krauss, and P. J. Renstrom, "Imprint lithography with 25-nanometer resolution," Science **272**(5258), 85–87 (1996).
20. Y. J. Lee, and S.-W. Kang, "Atomic layer deposition of aluminum thin films using an alternating supply of trimethylaluminum and a hydrogen plasma," Electrochem. Solid-State Lett. **5**(10), C91–C93 (2002).
21. K. C. Johnson, "GD-Calc," (2006)
22. *Handbook of optical constants of solids*, edited by E. D. Palik, Academic Press, (1985)

1. Introduction

Ultraviolet (UV) photodetection has a wide spectrum of applications, including detection of flame and electric discharge [1-2], early missile warning, chemical sensing [3], astronomical imaging [4] and covert communication [5-6], etc. Since UV light below 320 nm is strongly absorbed by the stratosphere, light detection in deep UV wavelength at the Earth surface has an extremely low background noise, if the visible and infrared radiation from the sun (longer than 320 nm) can be removed. This requires a solar-blind property, i.e. a high rejection ratio of visible and infrared light from the solar spectrum to deep UV light, in the UV detector.

Recently, there have been increasing research in the development of III-nitride materials based solar-blind UV photodetectors [7]. Significant effort has been devoted to overcoming the large lattice mismatch for growth of high quality $Al_xGa_{1-x}N$ on heterogeneous substrates such as sapphire. Despite the progress in photodetector and focal plane array imaging devices [8] based on III-nitride materials, technical challenges in achieving high-quality $Al_xGa_{1-x}N$ material growth are still significantly severe, hence greatly increasing the cost and limiting the detector's performance and detection area, as well as its applications. Other wide bandgap materials, such as SiC [9], $LaAlO_3$ [10], ZnO [11], diamond, etc., have also been demonstrated for use in solar-blind UV detection, but all of them are not compatible with conventional semiconductor processing and are difficult for integration with peripheral silicon-based electronics.

An alternative approach to solar-blind UV detection is to integrate Si-based photodetectors with solar-blind UV-pass filters to reject visible and IR light in the solar spectrum. This approach is particularly promising for large area imaging devices and for low-cost applications, since high performance Si photodetectors and large-area Si imaging devices have already been well developed and widely used. Several types of UV filters have been reported for solar-blind UV photodetection. Wood's filter uses a layer of alkali metal with high plasma frequency, such as Na, K and Li [4, 12], to block visible and infrared wavelength while pass UV light. However, besides the fixed cut-off wavelength determined intrinsically by material property, the usage of alkali metals brings other drawbacks to Wood's filter, such as contamination, poor robustness, environmental sensitivity, etc. Dielectric interference filters were also demonstrated for solar-blind UV applications [13], but this type of filter requires a thick stack of multiple dielectric material layers, that must be deposited with precise thickness and uniformity control and high quality over a very long deposition time [14], all of which inevitably increases production cost and reduces uniform area. Moreover, dielectric interference filters have the shortcomings of small acceptance angle and high sensitivity to environmental variation such as temperature and humidity.

In this paper, we will report design, fabrication, and characterization of a metal nano-grid deep-UV band pass filter, which is solar blind. Most earlier work on metal grid filters were in longer wavelengths such as THz [15], infrared [16], and visible [17] wavelength ranges, and had much larger grid geometry. Moreover, unlike previous metal nano-grid filters, which were fabricated by either electron beam lithography or multi-beam extreme UV (EUV) interference lithography [18] and therefore had a limited area and a high fabrication cost, our metal nano-grid filter was fabricated using nanoimprint lithography, featuring 190 nm pitch

#120565 - $15.00 USD Received 30 Nov 2009; revised 21 Dec 2009; accepted 21 Dec 2009; published 6 Jan 2010
(C) 2010 OSA

grid with 30 nm minimum feature size as well as high throughput and low cost production [19].

2. Device structure and fabrication

The structure of our metal grid filter consists of a dielectric grid array of periodic square holes on a UV transparent fused silica substrate and a thin aluminum layer coated over the dielectric grid, as shown in Fig. 1. This structure has several advantages over a solid aluminum grid in fabrication. The major advantage is that a high aspect ratio (>200 nm grid depth versus sub-50nm grid width) aluminum nano-grid is extremely challenging to fabricate, while a high aspect ratio dielectric nano-grid array is rather easy to fabricate and can have its dimensions well controlled. The critical geometric parameters of the UV pass filter, that determine the filter performance, are the grid period D, grid linewidth W and grid depth H, all of which can be defined by nanoimprint lithography and aluminum deposition. The structure can be viewed as an array of parallel metallic waveguides at nanoscale. Similar to RF waveguides, the nanoscale waveguides exhibit a cut-off wavelength above which no propagating optical mode exists therefore the transmission at long wavelength is suppressed. Aluminum is selected as the metal used to form the grid structure, solely for the reason that aluminum has a very high plasma frequency which makes it an excellent conductor at below 300 nm wavelength, which is important for our metal grid filter to work in the deep UV range.

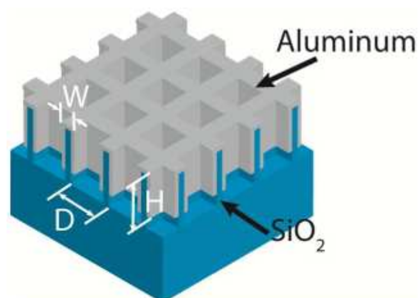

Fig. 1. Schematic of the metal nano-grid filter consisting of a dielectric grid array of periodic square holes on a UV transparent fused silica substrate and a thin aluminum layer coated over the dielectric grid.

Our device features a square dielectric core grid designed and fabricated with a pitch of 190nm, a linewidth of 30 nm and a depth of 250 nm. 20 nm thick Al was deposited obliquely on the grid sidewalls with a covered depth of about 200 nm. The geometric parameters of the dielectric core grid were chosen mainly according to our fabrication capability and also verified by numerical simulation for the desired pass band and transmission efficiency. The thickness of aluminum coating will affect the size of the opening area, therefore the cut-off wavelength and rejection ratio. Aluminum thickness of 20 nm was determined according to the desired filter performance and our fabrication feasibility.

Wafer-scale fabrication of this dielectric core grid structure with feature size as small as 30 nm is far beyond the capability of conventional lithography techniques, for example, photolithography is incapable of patterning sub-30 nm features and e-beam lithography may be too slow or too expensive to be used for wafer-scale patterning of high-density small features due to its low throughput. Therefore, nanoimprint lithography was used in our fabrication. The basic fabrication steps of the nano-grid filter included nanoimprint lithography using a narrow grating mold, etching of SiO_2 grid, and Al deposition. A key in the fabrication process was fabrication of the sub-30 nm SiO_2 square grid as the backbone for the Al grid. To fabricate this SiO_2 grid, we started with a 1D grating master mold and created 2D grid pattern in Cr by two cycles of nanoimprinting and Cr deposition and lift-off, with the direction of the 1D mold in the second cycle perpendicular to that in the first cycle. Figure 2 shows the flowchart of nanoimprint lithography based fabrication of our filter. The

#120565 - $15.00 USD Received 30 Nov 2009; revised 21 Dec 2009; accepted 21 Dec 2009; published 6 Jan 2010
(C) 2010 OSA

nanoimprint mold carrying the 1D grating patterns (Fig. 2(a)) was pressed into a thin layer of imprint resist spun on a UV-grade fused silica substrate as in Fig. 2(b). The grating width on the mold was shrunk to about 30 nm by HF etching of original 1:1 duty cycle SiO_2 gratings with precisely controlled time and rate. The imprinted resist pattern (Fig. 2(c)) was then transferred into underneath dielectric layer through a series of reactive ion etching (RIE) steps. The first RIE using O_2 plasma was to remove the residual layer of resist, and then 10 nm Cr was deposited by e-beam evaporation, as shown in Fig. 2(d). After subsequent lift-off process, a Cr grating was left on the substrate (Fig. 2(e)). By repeating the steps (a) through (d) with the grating mold rotated by 90°, a 2nd set of Cr grating, which is perpendicular to the 1st set of Cr grating pattern was fabricated on top of the substrate (Fig. 2(f)), forming a 2D Cr grid. Using this Cr grid as an etching mask, a 2nd CF_4/H_2 based RIE was used to transfer the grid pattern into the underneath fused silica substrate to form the 2D dielectric grid core as shown in Fig. 2 (g), after which aluminum was deposited on the sidewalls by oblique evaporations (Fig. 2(h)). The 2D grid fabricated in Fig. 2(g) can also be used as a mold for patterning 2D Cr masks on fused silica substrate in a single nanoimprint step to simplify device production.

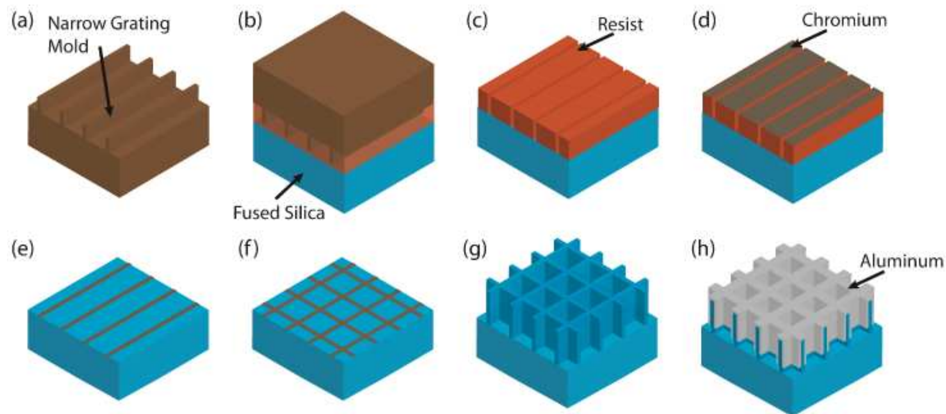

Fig. 2. Fabrication flowchart: (a) a silicon mold carrying narrow grating patterns with 190 nm pitch, 30 nm grating width and 120 nm depth; (b) pressing the mold into imprint resist spun on top of a fused silica wafer; (c) grating pattern transferred into imprint resist after separating the mold; (d) normal deposition of chromium after etching away residual resist in grating trenches; (e) 1st set of chromium grating etching mask after lift-off; (f) repeating (b)-(e) to get 2nd set of chromium grating etching mask which is perpendicular to the 1st set of chromium mask; (g) etching into fused silica substrate by CF_4/H_2 based RIE using the chromium grating in (f) as an etching mask; (h) oblique deposition of aluminum on the sidewalls of the fused silica grid core to form aluminum grid filter.

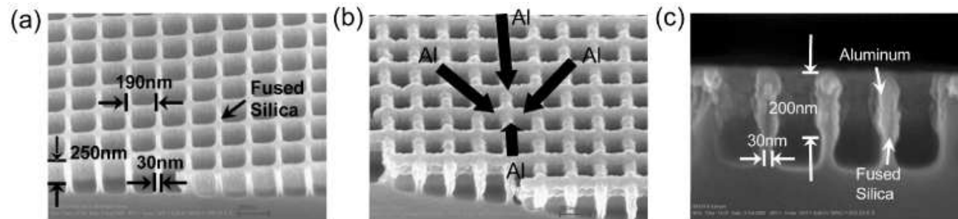

Fig. 3. SEM pictures of (a) SiO_2 grid core on fused silica substrate; (b) titled and (c) cross-sectional view of final device after coating 20 nm thick aluminum on the SiO_2 grid core.

SEM picture in Fig. 3(a) shows the fabricated dielectric grid core structure with a SiO_2 square grid of 190 nm period and 250 nm depth on fused silica substrate. By optimizing the RIE recipe, the large aspect ratio SiO_2 square grid was etched vertically and smoothly with an estimated sidewall surface roughness of less than 5 nm and maintained a uniform wall

#120565 - $15.00 USD Received 30 Nov 2009; revised 21 Dec 2009; accepted 21 Dec 2009; published 6 Jan 2010
(C) 2010 OSA

thickness of about 30 nm along up to 250 nm etched depth. Figure 3(b) and (c) show the aluminum deposited on the both sides of the SiO_2 grid by oblique e-beam evaporation from 4 opposite directions. The deposition angle was set to 40° so that the aluminum can cover about 200nm depth on the grid sidewall. The surface roughness after aluminum deposition is increased due to aluminum granules formed during deposition and the roughness can be reduced by using other conformal aluminum deposition methods, such as atomic layer deposition (ALD) [20].

3. Experimental characterization

The transmission of the fabricated filter was characterized in 200-700 nm range using a UV/visible spectrometer with an unpolarized incident light source. The measured transmission spectrum is shown in Fig. 4 (a) in linear scale, where a peak transmission efficiency of 27% is observed at 290 nm at normal incidence. The transmission drops to a half of the peak value at 350nm. For wavelengths longer than 480nm, the transmission is about 20dB lower than the peak transmission in deep UV range, indicating the rejection ratio of the deep-UV pass band wavelength to the longer visible wavelengths to be as high as 20dB.

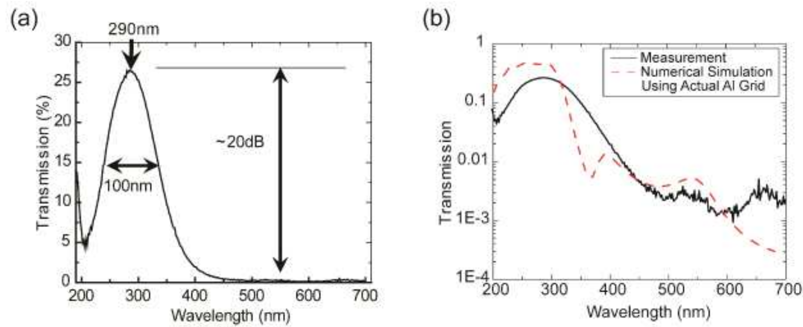

Fig. 4. (a) Measured transmission spectrum of a fabricated aluminum grid filter under unpolarized normal incidence (linear scale); (b) Comparison of measurement result and numerical simulation using actual structure dimensions. (logarithmic scale)

The measured results are compared with numerical simulation using actual structure dimensions in Fig. 4 (b) in logarithmic scale. The experimental measurements agree reasonably well with the numerical simulation results considering the fabrication imperfection in actual devices. The lower transmission and slightly red-shifted peak transmission wavelength and cut-off wavelength in measurement result are mostly caused by the rough surface on aluminum coatings.

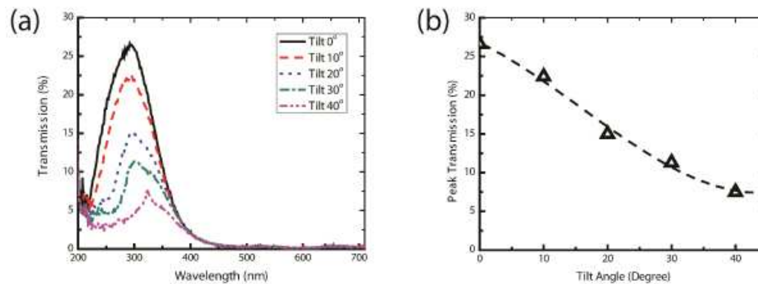

Fig. 5. (a) Measured transmission spectrum at various angles of incidence; (b) Measured peak transmission versus incident angle.

Since an ideal square grid filter has a symmetric shape, we expect the transmission through this UV filter has minimum polarization dependence. To test it, we used polarized incident light to measure the rejection ratio between the peak UV transmission wavelength

#120565 - $15.00 USD Received 30 Nov 2009; revised 21 Dec 2009; accepted 21 Dec 2009; published 6 Jan 2010
(C) 2010 OSA

and 543nm visible wavelength for two orthogonal polarization components, which were found to be 25dB and 21dB respectively. A 4-dB difference in the rejection ratio was observed for different polarization. This polarization-dependent rejection ratio is attributed to the asymmetry in the aluminum deposition process. During the four oblique aluminum deposition, the later depositions were affected by shadowing of earlier deposited aluminum, making the later aluminum coatings have less coverage on grid sidewalls and therefore resulting in slightly different rejection ratios for different polarizations. This can be further reduced by improving the oblique aluminum evaporation or adopting other aluminum deposition methods.

By tilting the fabricated filter in the measurement setup, we studied the effect of incident angle on the transmission efficiency, which may be important to certain wide angle imaging applications. Figure 5 shows the transmission spectra at different angle of incidence from 0° to 40°, from which we estimate that the filter has an acceptance angle of ±25° for transmission efficiency higher than half of the peak transmission.

4. Discussions

To better design and understand the metal grid structures, we used Rigorous Coupled Wave Analysis (RCWA) code GD-Calc [21] to model and simulate the transmission performance of the aluminum nano-grid filters with different geometric parameters. For simplicity, we used a solid aluminum grid structure, instead of aluminum grid coated on a dielectric core, in the RCWA simulation. Solid aluminum grid generally has better performance particularly on rejection ratio and is more desired despite of challenging fabrication. The refractive index of aluminum was taken from the experimentally measured data in [22], and we used a refractive index of 1.46 for SiO_2 in our simulation.

Figure 6(a) and (b) show the simulated transmission efficiency versus grid width and grid depth respectively for a solid aluminum square grid filter with 190 nm pitch. As shown in Fig. 6(a), with grid pitch fixed at 190 nm and grid depth at 300 nm, a wider aluminum grid width, i.e. smaller grid opening, results in shorter cut-off wavelength and lower transmission efficiency. Figure 6(b) demonstrates that, with all other parameters fixed, a deeper metal grid is required to achieve a higher rejection ratio between UV and visible light; specifically, with grid pitch fixed at 190 nm and grid width at 44nm which is comparable to the total aluminum thickness in our fabricated device, the grid depth needs to be at least 200nm to achieve >20dB rejection ratio between UV and visible wavelength range.

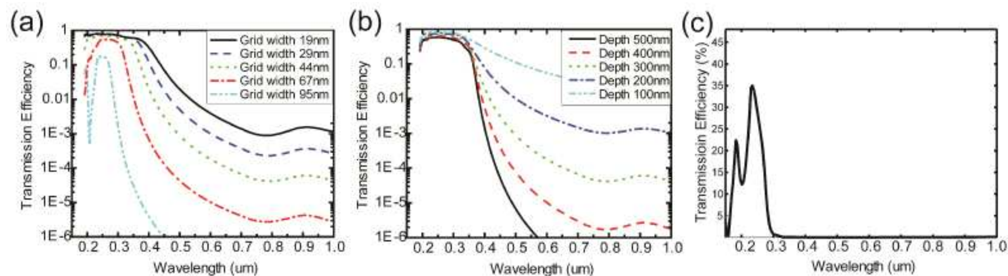

Fig. 6. (a) Simulated transmission efficiency versus aluminum grid width with the period fixed at 190nm and depth fixed at 300 nm; (b) Simulated transmission efficiency versus aluminum grid depth with the period fixed at 190nm and aluminum grid width fixed at 44 nm; (c) Pushing cut-off wavelength down to 280 nm by reducing the grid period to 140 nm and shrinking aluminum thickness to 20 nm.

To move the peak transmission further below current 290 nm, we need to shrink the grid opening by using smaller grid pitch. Figure 6(c) shows the simulation for an aluminum grid filter with a period of 140 nm and aluminum grid width of 20 nm, which has a peak transmission at 220 nm and a pass band width of about 100 nm (from 180 nm to 280 nm). To

#120565 - $15.00 USD Received 30 Nov 2009; revised 21 Dec 2009; accepted 21 Dec 2009; published 6 Jan 2010
(C) 2010 OSA

push the cut-off wavelength into shorter UV range, smaller periods and grid openings are needed for the nano-grid filter, which bring more challenges to the fabrication.

5. Conclusion

In summary, we designed, fabricated and demonstrated a solar-blind deep-UV pass filter that has a peak transmission of 27% at 290 nm, a pass band (at half maximum) from 250 to 350 nm and a rejection ratio to visible light of 20 dB. The filter has a unique structure of a 190 nm pitch dielectric grid core with 30 nm grid width and coated by 20 nm thick aluminum on each side of the grid. Nanoimprint lithography was used in fabrication of the dielectric grid core with high resolution on wafer scale area and oblique aluminum deposition by e-beam evaporation formed large-aspect-ratio aluminum grid on the dielectric core. This fabrication process demonstrates an IC-compatible and low-cost approach to metal grid filters working in solar blind UV range. Integrating the filter with Si photodetector or 2D Si imaging array allows compact, low-cost and large-area UV detection and imaging devices with solar-blind property.

Acknowledgement

The authors thank National Science Foundation (NSF) for a partial support to the research.